Cancer Therapeutic siRNA Delivery and Imaging by Nitrogen- and Neodymium-Doped Graphene Quantum Dots

Alina R. Valimukhametova,

Department of Physics and Astronomy, Texas Christian University, Fort Worth 76129, Texas, United States

Bong Han Lee,

Department of Physics and Astronomy, Texas Christian University, Fort Worth 76129, Texas, United States

Ugur C. Topkiran,

Department of Physics and Astronomy, Texas Christian University, Fort Worth 76129, Texas, United States

Klara Gries,

Department of Chemistry and Biochemistry, Heidelberg University, Heidelberg 69117, Germany

Roberto Gonzalez-Rodriguez,

Department of Physics, University of North Texas, Denton 76203-1277 Texas,, United States

Jeffery L. Coffer,

Department of Chemistry and Biochemistry, Texas Christian University, Fort Worth 76129 Texas, United States

Giridhar Akkaraju,

Department of Biology, Texas Christian University, Fort Worth 76129 Texas, United States

Anton Naumov

Department of Physics and Astronomy, Texas Christian University, Fort Worth 76129, Texas, United States

Abstract

Corresponding Author Anton Naumov – a.naumov@tcu.edu.
Author Contributions
All authors have given approval to the final version of the manuscript.

ASSOCIATED CONTENT
Supporting Information
The Supporting Information is available free of charge at https://pubs.acs.org/doi/10.1021/acsbiomaterials.3c00369.

Figure S1, TEM images and size distributions of NGQD and Nd-NGQDs; Figure S2, EDX spectra of Nd-NGQDs; Figure S3, FTIR spectra of NGQDs and Nd-NGQDs; Figure S4, UV–vis absorption spectra of NGQDs and Nd-NGQDs and NIR absorption spectra of Nd-NGQDs; Figure S5, gel retardation assay of NGQD/siEGFR and Nd-NGQD/siKRAS complexes at different weight ratios; Figure S6, HRTEM and TEM images of NGQD/siEGFR complex at a 1:0.01 weight ratio; Figure S7, DLS spectra of NGQDs, NGQDs/siEGFR, and NGQDs/siKRAS; and Figure S8, western blots of NGQDs and Nd-NGQDs at 375 μg/mL concentration (PDF)

Complete contact information is available at: https://pubs.acs.org/10.1021/acsbiomaterials.3c00369

The authors declare no competing financial interest.

While small interfering RNA (siRNA) technology has become a powerful tool that can enable cancer-specific gene therapy, its translation to the clinic is still hampered by the inability of the genes alone to cell transfection, poor siRNA stability in blood, and the lack of delivery tracking capabilities. Recently, graphene quantum dots (GQDs) have emerged as a novel platform allowing targeted drug delivery and fluorescence image tracking in visible and near-infrared regions. These capabilities can aid in overcoming primary obstacles to siRNA therapeutics. Here, for the first time, we utilize biocompatible nitrogen- and neodymium-doped graphene quantum dots (NGQDs and Nd-NGQDs, respectively) for the delivery of Kirsten rat sarcoma virus (KRAS) and epidermal growth factor receptor (EGFR) siRNA effective against a variety of cancer types. GQDs loaded with siRNA noncovalently facilitate successful siRNA transfection into HeLa cells, confirmed by confocal fluorescence microscopy at biocompatible GQD concentrations of 375 μg/mL. While the GQD platform provides visible fluorescence tracking, Nd doping enables deeper-tissue near-infrared fluorescence imaging suitable for both *in vitro* and *in vivo* applications. The therapeutic efficacy of the GQD/siRNA complex is verified by successful protein knockdown in HeLa cells at nanomolar siEGFR and siKRAS concentrations. A range of GQD/siRNA loading ratios and payloads are tested to ultimately provide substantial inhibition of protein expression down to 31–45%, comparable with conventional Lipofectamine-mediated delivery. This demonstrates the promising potential of GQDs for the nontoxic delivery of siRNA and genes in general, complemented by multiwavelength image tracking.

Keywords

siRNA delivery; graphene quantum dots; near-infrared fluorescence; confocal microscopy; EGFR; KRAS

1. INTRODUCTION

Cancer is a life-threatening disease that affects more than one million people yearly in the United States alone.[1,2] Pathological conditions associated with cancer result from the accumulation of multiple mutation-associated genetic and epigenetic changes.[3] Genetic mutations lead to the dysregulation of a variety of proteins in different forms of cancer.[4] For instance, epidermal growth factor receptor (EGFR) and Kirsten rat sarcoma virus (KRAS) genes are frequently mutated in nonsmall lung cancer.[5,6] Targeting EGFR and KRAS may provide an approach to lung cancer treatment as they play a crucial role in carcinogenesis, causing sustained proliferation of cells.[7,8] Although EGFR responds well to tyrosine kinase inhibitor (TKI) therapy, drug resistance remains a major issue.[9] According to recent studies, EGFR resistance to TKI therapy can be caused mainly by KRAS mutations, as KRAS is a downstream effector in EGFR signaling.[10] At the same time, KRAS is resistant to most available therapeutics and is difficult to target, making both EGFR and KRAS desired critical targets for cancer gene therapy.[6,11]

In the last decade, RNA interference (RNAi)-based therapeutics have attracted substantial attention in cancer therapy.[12] One of the major types of RNAi technology includes the delivery of small interfering RNAs (siRNAs), noncoding double-stranded oligos roughly 20–24 nucleotides in length. Unlike tyrosine kinase inhibitors that can act on multiple targets

and may lack specificity,[13] siRNA binds to a specific complementary mRNA sequence, inducing its cleavage and inhibiting corresponding protein synthesis.[14] To date, the FDA has already approved four siRNA-based treatments, making RNAi technology a prospective tool in gene silencing.[15] However, as a therapeutic method, RNAi technology is hampered by the inability of siRNA to transfect cells on its own and its rapid enzymatic degradation in bodily fluids and tissues.[16] In order to overcome these obstacles, both viral and nonviral delivery vehicles have been developed.[17] While highly effective, viral delivery vehicles can provoke a strong immune response, whereas their nonviral counterparts are considered more safe and more versatile.[18,19] For example, several types of lipid-based nanoparticles have already been approved by FDA for drug delivery[20] and demonstrate high transfection efficacy. In order to enable gene therapy to its fullest extent, modern nanocarriers have to protect the siRNA from serum nucleases, target the disease site to ensure high therapeutic accumulation and effective release, overcome biological barriers hampering gene transfection, facilitate endosomal escape, and possess delivery tracking capabilities.[21] In this capacity, solid nanoparticles are often more beneficial than their organic counterparts such as liposomes due to higher physical stability; versatile surface chemistry; tunable optical properties; and their potential for multimodality in delivery, targeting, and image-based detection.[22,23]

Among solid nanoparticles, gold nanoconstructs have been used for siRNA transport due to their high biocompatibility, monodispersity, and the ability for surface modification.[24] In several recent works, gold nanoparticles conjugated with polyethylenimine (PEI) provide high gene transfection efficiency.[25,26] PEI is known to increase electrostatic interaction with siRNA and facilitate its internalization through the cell membrane and endosomal escape. However, on its own, PEI exhibits significant cellular toxicity,[27] hampering the use of PEI-decorated nanoparticles in the clinic. Thus, the nontoxic incorporation of nitrogen groups within the nanomaterial is a highly desired option. Carbon-based nanomaterials, such as single-walled carbon nanotubes (SWCNTs), can also serve as carriers for gene delivery.[28,29] Due to their physical properties, SWCNTs can enter cells, while their hexagonal carbon rings allow for noncovalent therapeutic loading. Additionally, SWCNTs exhibit intrinsic fluorescence in the near-infrared (NIR) spectral region, providing drug/gene delivery tracking capabilities.[30] Low biological autofluorescence, tissue absorption, and scattering in the NIR enhance the applicability of such image tracking ability to *in vivo* models.[31] SWCNTs can carry siKRAS and siEGFR and facilitate efficient knockdown of both target proteins *in vitro* and *in vivo*.[32] This leads to substantial inhibition of the cancer tumor growth rate, while the intrinsic SWCNT NIR fluorescence verifies the delivery of SWCNT/siRNA complexes in biological cells and tumor tissues. SWCNT-based platforms are also explored for siRNA delivery in intact plant cells.[33] Another carbon-based nanomaterial, graphene oxide (GO), can also serve as a multifunctional platform for gene delivery, imaging, and cancer sensing.[34] The GO surface can be modified with positively charged moieties in order to ensure siRNA loading.[35,36] While all aforementioned nanomaterials can be prospective platforms for siRNA delivery, their toxicity at low concentrations, long-term tissue accumulation, and complex synthesis[37,38] can limit them from proceeding to mass production and clinical studies.

In the last decade, yet other carbon nanomaterials, graphene quantum dots (GQDs), have emerged as a promising carrier for gene delivery.[39,40] GQDs are zero-dimensional

nanostructures consisting of a few layers of graphene sheets with lateral dimensions generally below 20 nm. There are two routes to GQD synthesis, "top-down", which is based on the decomposition of larger graphene-based materials into nanometer-scale GQDs, and "bottom-up", involving further carbonization of small carbon-containing molecules used as precursor materials.[41] Due to the presence of a carbon lattice and, often, oxygen functional groups, GQDs can bind a variety of molecules through π–π stacking or electrostatic interactions. Oxygen addends also allow for covalent functionalization.[39] These properties render GQDs ideal candidates for the delivery of different therapeutic platforms. Compared to the SWCNTs and GO, GQDs exhibit minimal toxicity *in vitro* and *in vivo* due to their smaller size and rapid excretion.[42] They can successfully deliver several drug and gene payloads.[43–45] In addition to being a delivery agent, GQDs can also be utilized for imaging and biosensing. They are photostable and exhibit intrinsic fluorescence in the visible (VIS) and NIR regions, which can serve as a noninvasive detection mechanism.[46,47] Several GQD-based optical sensors have recently been developed for the detection of RNA,[48] ssDNA,[49] miRNA,[50] proteins,[51] and small molecules.[52,53] The successful siRNA delivery capability is recently shown by the GQDs synthesized by the bottom-up approach from glucose and tetraethylene pentaamine.[54] Loaded with both an aptamer and siRNA, GQDs can improve the efficiency of siRNA internalization into hepatocellular carcinoma cells, inhibiting the expression of Fragile X mental retardation protein.[55] Similar to other nanoparticles, when conjugated with PEI, GQDs exhibit enhanced siRNA loading via the electrostatic interaction of the negatively charged gene with the cationic polymer.[56–58] Facile synthesis, versatility of design and functionalization, and their optical properties can allow GQDs to address the critical needs in gene delivery and imaging. Enhancing their biocompatibility and image tracking modalities can facilitate the progression of this platform toward *in vivo* applications. Developed in our previous work,[59,60] nitrogen-doped and neodymium-doped graphene quantum dots (NGQDs and Nd-NGQDs, respectively) possess these desired capabilities. They are biocompatible at up to 1 mg/mL concentrations and exhibit high (8–62%) quantum yield fluorescence in visible and near-infrared regions. In fact, the NIR fluorescence arising from Nd dopants in Nd-NGQDs can be successfully utilized for *in vivo* animal imaging of live mice without their dissection. NGQDs having nitrogen functional groups on their surface show the capacity for noncovalent gene attachment, forming stable complexes with adsorbed ssDNA.[50] These properties suggest that NGQDs and Nd-doped NGQDs can be perspective platforms for image-guided siRNA delivery.

To test this, we have for the first time utilized biocompatible NGQDs and Nd-NGQDs for the delivery and imaging of KRAS and EGFR siRNAs in HeLa cells. Unlike previously developed platforms for siRNA delivery,[56–58] NGQDs and Nd-NGQDs are synthesized by a one-step microwave-assisted hydrothermal method that does not contain any substantially toxic precursors, thereby rendering these GQDs biocompatible and simple in production. Moreover, NIR fluorescent GQDs that can offer the advantage of *ex vivo* and *in vivo* tracking have not been previously utilized for gene delivery or imaging. This work, therefore, explores unique anticancer therapeutic siRNA delivery platforms that possess a promising potential for translating siRNA technology into the clinic.

2. MATERIALS AND METHODS

2.1. Synthesis of NGQDs and Nd-NGQDs.

In order to produce nitrogen-doped graphene quantum dots (NGQDs) and neodymium-doped graphene quantum dots (Nd-NGQDs),[59,60] 4 g of glucosamine hydrochloride (104K0082, Sigma-Aldrich) was dispersed in 250 mL of deionized (DI) water. For Nd-NGQDs, $Nd(NO_3)_3 \cdot 6H_2O$ (MKCH8576, Sigma-Aldrich) was added in powder form, yielding a final 0.008 M concentration. The mixture was microwaved in an HB-P90D23AP-ST Hamilton Beach microwave oven for 60 min at 1350 W power. During microwave synthesis, we observed boiling of the mixture followed by an up to three times decrease in volume. After the synthesis, samples were cooled down and transferred to a 1 kDa molecular weight cutoff dialysis bag for 24 h dialysis against DI water to remove unreacted material. DI water was changed every 30 min for the first 3 h and every 7 h for the next 21 h. Then, all of the samples were sterilized using a 0.22 μm syringe filter. Part of the product was freeze-dried in order to define the concentration, and the products were further air-dried to adjust the concentration to ~10 mg/mL.

2.2. Complexation of NGQDs and Nd-NGQDs with siRNAs.

To load siKRAS and siEGFR (Nitto Avecia Inc.) onto both types of GQDs, 75 μL (750 μg) of 10 mg/mL GQD suspension was mixed with 0.5, 1, 5, 10, and 15 μL of siKRAS or siEGFR stock solution (15 μg/μL (1 nmol/μL) in DEPC-treated water) and incubated for 10 min at room temperature to produce GQD/siRNA complexes at weight ratios of 1:0.01, 1:0.02, 1:0.1, 1:0.2, and 1:0.3. For the cell internalization microscopy experiment, NGQD/siRNA or Nd-NGQD/siRNA hybrids were prepared at 375 μg/mL GQD concentration and 1:0.01 weight ratio with carboxy-X-rhodamine (ROX)-tagged siEGFR (5′-GUCGCUAUCAAGGAAUUAAdTdT-3′) and siKRAS (5′-CGAAUAUGAUCCAACAAUAdTdT-3′) genes to form NGQDs/siEGFR-ROX, NGQDs/siKRAS-ROX, Nd-NGQDs/siEGFR-ROX, or Nd-NGQDs/siKRAS-ROX.

2.3. Structural/Optical Characterizations (HRTEM/TEM, EDS, FTIR, Absorbance, Fluorescence, and ζ Potential).

The morphological characterization of NGQDs, Nd-NGQDs, and the NGQD/siEGFR complex was performed by HRTEM (high-resolution transmission electron microscopy, JEOL JEM-2100) with energy-dispersive X-ray analysis (EDS, JEOL, Peabody, MA). The samples were air-dried on a carbon-coated 200-mesh copper grid. To assess the functional groups of NGQDs and Nd-NGQDs, the samples were analyzed via the ATR mode of a Thermo Nicolet Nexus 670 FTIR after freeze-drying in a Labconco FreeZone 4.5 freeze dryer. The absorbance of NGQDs and Nd-NGQDs was measured within the range of 200–1000 nm by an Agilent Technologies Cary 60 UV–vis absorption spectrometer. Photoluminescence spectra of NGQDs and Nd-NGQDs in the visible and NIR regions were collected by a Horiba Scientific SPEX NanoLog spectrofluorometer. Fluorescence microscopy imaging was performed using an Olympus IX73 fluorescence microscope with a 60× (IR-corrected Olympus Plan Apo) water immersion objective coupled to a Photometrics Prime 95B CMOS camera with an Olympus DSU (disk spinning unit) confocal system for visible imaging. Excitation/emission filter wheels enabled spectrally resolved image

acquisition. An optimal configuration of filters was selected based on GQD (480 ± 20 nm excitation and 535 ± 20 nm emission filters) and ROX (540 ± 20 nm excitation and 605 nm emission filters) emission spectra. Spectrally resolved imaging in the near-infrared region (850–1600 nm) was enabled by the NIR InGaAs Photon etc. (ZephIR 1.7) detector coupled to the microscope through a hyperspectral fluorescence imager (Photon etc.). ζ Potentials of GQDs and NGQDs/siEGFR, NGQDs/siKRAS, Nd-NGQDs/siEGFR, and Nd-NGQD/siKRAS complexes at 1:0.01 w/w ratios were measured to evaluate the net charge of these in aqueous suspensions using a NanoBrook ZetaPALS instrument. The same instrument was used to measure dynamic light scattering (DLS) of NGQDs, NGQDs/siEGFR, and NGQDs/siKRAS at 1:0.01 w/w ratios.

2.4. Gel Retardation Assay.

NGQDs and Nd-NGQDs in water suspensions were mixed with siEGFR and siKRAS at various weight ratios (0:1, 1:2, 1:1, 1:0.3, 1:0.2, 1:0.1, 1:0.02, 1:0.01) while maintaining the concentration of siEGFR and siKRAS constant (0.375 μg/μL). The resulting samples were incubated for 10 min, mixed with 1× BlueJuice DNA loading buffer (10816015, Invitrogen), loaded onto 1.75% (w/v) agarose gel, and run in Tris–borate–EDTA (TBE) buffer at 80 V for 45 min. After electrophoresis, gels were stained with 0.5 μg/mL ethidium bromide solution (20F1056078, Invitrogen) in TBE buffer for 20 min on an orbital shaker. To reduce background signals, the agarose gel was further destained in TBE buffer for 5 min on an orbital shaker, after which all of the gels were imaged using a FastGene FAS-V Imaging System.

2.5. Cell Culture.

HeLa cells were cultured in Dulbecco's modified Eagle's medium (D6046, Sigma-Aldrich) and 10% fetal bovine serum (16140–063, Gibco) with the addition of 1% L-glutamine (G7513, Sigma-Aldrich), minimum essential medium (MEM) nonessential amino acid solution (M7145, Sigma-Aldrich), and penicillin/streptomycin (P4333, Sigma-Aldrich). The cell culture was kept in an incubator with 5% CO_2 at 37 °C and used for the cell viability assay, cell internalization microscopy study, and western blot analysis.

2.6. MTT Assay.

HeLa cells were plated at 5×10^3 cells per well in a 96-well plate and allowed to attach overnight. The cells were further treated with NGQDs/siEGFR, NGQDs/siKRAS, Nd-NGQDs/siEGFR, or Nd-NGQDs/siKRAS at a weight ratio of 1:0.01 with different concentrations of NGQDs and Nd-NGQDs. After 48 h incubation, the medium was replaced by 100 μL of 1 mg/mL 3-(4-dimethylthiazol-2-yl)-2,5-diphenyltetrazolium bromide (MTT). After 4 h of further incubation, MTT was replaced with 100 μL of dimethyl sulfoxide (DMSO) to dissolve blue formazan formed in the metabolically active cells. The characteristic formazan absorbance was measured on a microplate reader (FLUOstar Omega) at 580 nm and considered proportional to the number of alive cells.

2.7. Cell Internalization of NGQD/ROX-siEGFR, NGQD/ROX-siKRAS, Nd-NGQD/ROX-siEGFR, or Nd-NGQD/ROX-siKRAS Complexes.

The cell internalization microscopy experiment assessed the internalization of NGQD/siRNA or Nd-NGQD/siRNA hybrids. HeLa cells were seeded at 1×10^4 cells onto a glass coverslip placed in a six-well plate overnight. The cells were treated with NGQDs/siEGFR-ROX, NGQDs/siKRAS-ROX, Nd-NGQDs/siEGFR-ROX, or Nd-NGQDs/siKRAS-ROX for 12 h. The coverslips with cells were further washed with $1\times$ phosphate-buffered saline (PBS) to remove GQD/siRNA complexes that did not internalize. Cells were fixed with 4% formaldehyde solution (28908, Thermo Scientific) and $1\times$ Fluoromount-GTM mounting medium (00–4958-02, Invitrogen) and sealed onto microscope slides for imaging with an Olympus IX73 fluorescence microscope with aforementioned visible and NIR detection systems.

2.8. Western Blot Analysis.

HeLa cells were plated at 1.8×10^5 cells per well in a six-well plate and allowed to attach overnight. The cells were transfected with NGQDs/siEGFR, NGQDs/siKRAS, Nd-NGQDs/siEGFR, or Nd-NGQDs/siKRAS at different ratios following the procedure in Section 2.2, as well as with Lipofectamine 3000 (L3000001, Invitrogen) delivering siKRAS or siEGFR as per the manufacturer's protocol. After 24 h, cells were washed with a fresh complete medium and left for an additional 24 h of incubation. After that, the cells were washed with room-temperature phosphate-buffered saline (PBS) and directly lysed in RIPA lysis buffer (20–188, Millipore Sigma) supplemented with protease and phosphatase inhibitor cocktails (11836153001 and 04906845001, Roche). All of the proteins were extracted and quantified by the Bradford protein assay using bovine serum albumin (BSA) as a standard. The proteins were further mixed with SDS loading buffer (BioRad) and heated for 10 min at 95 °C. Equal amounts of proteins were electrophoresed in 10% TGX stain-free acrylamide gel (1610182, BioRad) at 100 V for 1.5 h and transferred onto a nitrocellulose membrane (88018, Thermo Scientific) at 25 V and 1.0–1.3 A using a Trans-Blot Turbo transfer system apparatus (1704150, BioRad). Membranes were blocked with blocking buffer (3% BSA in TBS-T (Tris-buffered saline with 0.1% Tween 20 detergent, BioRad)) for 1 h and incubated with primary antibodies (Actin, Santa Cruz Biotech sc-8432, 1:1000 dilution; KRAS, sc-30, 1:200 dilution; EGFR, sc-365829, 1:200 dilution) in the blocking buffer overnight at 4 °C. After that, membranes were washed with blocking buffer three times and incubated with a secondary antibody (1706516, BioRad, 1:3000 dilution) for 1–2 h. Actin was used as a control to ensure that an equal amount of protein was loaded in each line. After washing, membranes were stained with the Opti-4CN Substrate Kit (1708235, BioRad) and imaged using a FastGene FAS-V Imaging System.

2.9. Geometry Optimization.

The structure of the NGQD/siEGFR complexes was investigated by the energy minimization method through the auto-optimization tools within Avogadro software.[61] Merck Molecular Force Field 94 (MMFF94)[62] was chosen as it is best utilized with organic materials such as NGQDs and siRNAs. Moreover, the steepest descent optimization algorithm was used with an energy convergence of 10^{-6} units at a 2500 step limit to provide the best

structural assessment. The center flake of the multilayer NGQDs was built in accordance with previous theoretical modeling of the NGQD structures based on the percentages of oxygen and nitrogen-containing functional groups.[63] Other GQD planes were derived from the central and separately optimized before final geometrical optimization with the siRNA. The exact siEGFR sequence used for fluorescence imaging in this work is presented in the model.

3. RESULTS AND DISCUSSION

In this work, a novel avenue for siRNA cancer gene therapy is explored with NGQD and Nd-NGQD carrier/imaging platforms synthesized using a microwave-assisted hydrothermal method with a glucosamine carbon precursor. Upon microwave treatment, glucosamine molecules undergo a hydrothermal reaction and form aromatic clusters, serving as nucleation centers for the formation of NGQDs. With the addition of the $Nd(NO_3)_3 \cdot 6H_2O$ salt to the reaction mixture, neodymium ions dope the nucleating NGQDs, leading to the formation of Nd-NGQDs. The morphologies and structures of the purified and filtered NGQDs and Nd-NGQDs are characterized by TEM and HRTEM. Both samples contain evenly distributed GQDs with respective average diameters of 4.0 ± 0.6 and 3.8 ± 0.9 nm (Figure S1). HRTEM images (Figure 1) of NGQDs and Nd-NGQDs reveal their graphitic structure demonstrating characteristic graphene lattice fringes[64] with respective interplanar spacings of 0.26 ± 0.03 and 0.21 ± 0.03 nm, while the fast Fourier transform (FFT) images confirm their crystallinity. EDX analysis is performed to ensure the presence of Nd in Nd-NGQDs after purification and filtration, removing unreacted Nd precursors (Figure S2). EDX spectra demonstrate ~1 atom % of Nd in Nd-NGQDs, confirming their successful doping. Due to its small amount, the metal dopant is not expected to affect the biocompatibility of the GQDs.[65] Besides Nd, EDX analysis indicates carbon, oxygen, and nitrogen, suggesting the presence of various functional groups in the GQD structure. FTIR spectra of freeze-dried GQD samples (Figure S3) indicate that hydroxyl, carboxyl, and amino groups are most likely present on the surface of the GQDs, enabling high water solubility as well as complexation with nucleic acids[50] and covalent functionalization for biological applications.[66] In this work, several modalities of these GQD platforms are tested to identify their capability for successful siRNA delivery.

In order to assess the imaging capabilities of the GQD platforms, their optical properties are evaluated via absorbance and fluorescence spectroscopy techniques. Absorption spectra of NGQDs and Nd-NGQDs (Figure S4a) show dominant features at ~200 and ~276 nm, which are ascribed to π–π* and n–π* electronic transitions of the C═C and C═O bonds, respectively. The shoulder at ~317 nm is attributed to the π–π* transition of the C═N bond.[67] These spectral features are exclusive to the NGQDs and are not present in the spectrum of glucosamine (Figure S4a). Nd-NGQDs also possess an absorption peak at ~800 nm (Figure S4b) corresponding to the $^4I_{9/2} \rightarrow {}^4F_{5/2}$ transition of the Nd^{3+}, enabling their fluorescence excitation with an 808 nm laser. With this excitation, Nd-NGQDs exhibit several emission features at ~900, 1060, and 1330 nm (Figure 2a) attributed to the $^4F_{3/2} \rightarrow {}^4I_{9/2}$, $^4F_{3/2} \rightarrow {}^4I_{11/2}$, and $^4F_{3/2} \rightarrow {}^4I_{13/2}$ neodymium(III) electronic transitions, respectively, verifying the capability of Nd-NGQDs for deep-tissue NIR imaging.[60] Both NGQDs and Nd-NGQDs exhibit fluorescence in the visible region (Figure 2b). Upon excitation with

400 nm, both samples show a similar broad emission peak at ~500 nm ascribed to the quantum confinement-originating intrinsic GQD fluorescence.[63] The width of the spectrum is attributed to the distribution of different GQD sizes in the sample with a variety of size-dependent emission wavelengths. While visible fluorescence is not commonly used for *in vivo* applications, it provides an essential *in vitro* imaging modality, enabling the tracking of the internalization of the GQDs into biological cells. Overall, the visible and NIR fluorescence capabilities of NGQDs and Nd-NGQDs make them prospective nanomaterials for *in vitro* and *in vivo* bioimaging applications.

The capabilities of NGQDs and Nd-NGQDs to complex siRNA for its delivery were assessed via ζ potentials and gel retardation assays. Both NGQDs and Nd-NGQDs show positive ζ potentials (1.8 ± 0.7 and 8.3 ± 0.7 mV, respectively), indicative of their positive surface charge (Figure 3a), attributed mainly to amino groups on the GQD surface. Incorporation of Nd^{3+} into the Nd-NGQD structure and the positive defects created by doping can be deemed responsible for the elevated ζ potential of the Nd-NGQDs.[68] Utilizing positively charged GQDs can facilitate more effective binding of the siKRAS and siEGFR genes that possess negative ζ potentials (-18.8 ± 1.4 and -9.9 ± 0.8 mV, respectively) and are negatively charged due to the presence of phosphate groups. Given this electrostatic binding advantage, the loading capacity of both genes onto NGQDs and Nd-NGQDs was evaluated via the gel retardation assay (Figures 3b and S5). In this assay, each GQD type and each gene are mixed together in an aqueous suspension at the weight ratios of 0:1, 1:2, 1:1, 1:0.3, 1:0.2, 1:0.1, 1:0.02, and 1:0.01 at a final volume of 20 μL and incubated for 10 min at room temperature to allow complexation. When loaded onto the gel, the complex with lower mobility is likely to be more neutral, which is expected from a most efficient combination of positively charged GQDs and negatively charged siRNAs.[69] The results of the gel retardation assay demonstrate that the migration of siEGFR and siKRAS gradually decreases with increasing GQD/siRNA ratio. The maximum band "shift" with respect to the control column (0:1), which contains only negatively charged siRNA, was observed at a GQD/siRNA weight ratio of 1:0.01, indicating efficient complexation of siRNAs and GQDs at this ratio. ζ potentials of the Nd-NGQDs/siEGFR and Nd-NGQDs/siKRAS at that weight ratio are measured to be positive (0.8 ± 0.3 mV and 5.1 ± 0.6 mV, respectively), giving a promise for effective cell entry and endosomal escape.[70] NGQDs/siEGFR and NGQDs/siKRAS demonstrate negative ζ potentials (-6.9 ± 0.6 mV and -4.4 ± 1.1 mV, respectively) due to the initial lower charge of the NGQDs with the same amount of siRNA complexed. Similar potentials were previously observed for the NGQD platform with absorbed single-stranded DNA for miRNA detection.[50] The change in the net electric charge of all complexes confirms the electrostatic interaction between the GQDs and siRNAs. While having positively charged nanoparticles may pose a substantial advantage for internalization, negatively charged GQDs may appear to enter the cells via an entirely different internalization mechanism.[71] In the case of cationic GQDs, micropinocytosis is considered a major internalization pathway, while anionic GQDs are known to internalize mostly through caveolae-mediated and clathrin-mediated endocytosis.[71,72] Thus, despite their charge, both NGQD/siRNA and Nd-NGQD/siRNA complexes have a potential for gene delivery.

Following up on the ζ potential results, we performed geometry optimization calculations with the MMFF94 force field (Figure 4), which demonstrates a plausible configuration of the NGQD/siEGFR complex. Electrostatic interactions between the GQDs and the gene can arise from the alignment of positively charged amino groups of the NGQDs and negatively charged siRNA phosphate groups at the biological pH (Figure 4, inset). The calculation shows the potential of successfully complexing several GQD structures with a larger siRNA sequence. Experimentally, as expected from the simulation, HRTEM and TEM images of the NGQD/siEGFR complex show bigger structures compared to individual GQDs, indicating successful siEGFR adsorption onto the NGQD surface (Figure S6). According to the DLS analysis (Figure S7), the average size of NGQDs increases from 2.55 nm to 12.52 and 11.15 nm after complexation with siEGFR and siKRAS, respectively. After complexation assessment, different weight ratios are further tested for gene delivery in HeLa cells.

Maximum biocompatible concentrations for intracellular delivery of siRNA are determined in this work via the MTT cytotoxicity assay. Due to the low cytotoxicity of the precursor material and only small percent metal doping, both NGQDs and Nd-NGQDs are expected to exhibit biocompatibility at high concentrations. In order to select the highest biocompatible concentration for imaging and delivery, HeLa cells were treated with NGQD/siEGFR, NGQD/siKRAS, Nd-NGQD/siEGFR, and Nd-NGQD/siKRAS complexes for 48 h at different amounts of NGQDs and Nd-NGQDs (Figure 5a,b). Both complexes demonstrate ~70 to 80% cell viability at a GQD concentration of 375 μg/mL with a GQD/siRNA w/w ratio of 1:0.01, indicating that minor Nd doping does not contribute to the toxicity profile of the formulation.

Confocal fluorescence microscopy is utilized in this work to assess the delivery of siEGFR and siKRAS into HeLa cells by the GQDs. Both siEGFR and siKRAS were labeled with ROX and complexed with either NGQDs or Nd-NGQDs to form four combinations: NGQDs/siEGFR-ROX, NGQDs/siKRAS-ROX, Nd-NGQDs/siEGFR-ROX, and Nd-NGQDs/siKRAS-ROX. These complexes were left to transfect HeLa cells for 12 h, which has been previously determined as an optimal internalization time for both GQD types.[59,65] In order to separately image fluorescence from GQDs and ROX, these were spectrally separated by exciting at 480 and 540 nm, respectively, with the corresponding emission recorded at 535 ± 20 and 600 ± 20 nm (Figure 6). Confocal images taken at a median plane within the cells demonstrate only fluorescence from the internalized GQDs and siRNA-ROX, disregarding those accumulated on the cell membrane. The noninternalized GQD/siRNA complexes have been removed via a washing procedure. Considering substantial green GQD fluorescence and ROX emission observed within the cells (Figure 6), we infer that these complexes successfully transfected the cells. This is further confirmed by reconstructing a 3D image of fluorescence within the cells (Figure 6b, inset) from individual imaging planes by z-stacking. The resulting red and green fluorescence filling the cell demonstrates the presence of both NGQDs and siKRAS-ROX within HeLa cells. As anticipated, NGQDs and Nd-NGQDs are mostly localized in the cytoplasm of HeLa cells,[73] while siEGFR and siKRAS are also present in the cytoplasm and can be translocated into the nucleus.[74] NIR emission from Nd-NGQDs within the HeLa cells collected via hyperspectral microscopy with 808 nm excitation further confirms their successful internalization and potential for NIR imaging applications *in vivo*. These results

verify the successful transfection of GQD/siRNA complexes into HeLa cells; however, these do not provide the proof of their therapeutic efficacy.

In order to evaluate the gene silencing ability of GQD/siRNA complexes, the corresponding protein expression levels were assessed via western blot analysis. NGQDs and Nd-NGQDs at biocompatible 375 μg/mL concentrations were set to transfect HeLa cells for 48 h to ensure the platforms do not dysregulate the expression of EGFR and KRAS proteins. At that point, no change in protein expression with respect to the untreated blank control group (Figure S8) was observed, suggesting that the therapeutic contribution of the GQDs is negligible. It has been previously shown that once a platform is introduced into biological systems, proteins in the biological fluid can spontaneously adsorb to the nanoparticle surfaces and, in some instances, displace loaded genes.[75] Thus, in order to fully investigate the therapeutic efficiency of NGQDs/siEGFR, Nd-NGQDs/siEGFR, NGQDs/siKRAS, and Nd-NGQDs/siKRAS, these complexes were further tested in a cellular environment. Exposing HeLa cells to NGQD/siEGFR, Nd-NGQD/siEGFR, NGQD/siKRAS, or Nd-NGQD/siKRAS complexes at different weight ratios but at a constant 375 μg/mL GQD concentration shows a pattern of protein inhibition for all four complexes. Lipofectamine 3000, known to facilitate successful siRNA transfection, is used as a positive control, delivering 0.25 nmol/mL of each siRNA. Actin is utilized as a protein expression control, as it is expressed within all eukaryotic cell types and is usually not affected by cellular treatments.[76] As a result, NGQD/siEGFR and Nd-NGQD/siEGFR complexes facilitate the reduction of the EGFR expression level down to 31.3 ± 8.0 and $36.0 \pm 7.5\%$ at the 1:0.1 and 1:0.01 GQD/siRNA weight ratios, respectively (Figure 7a). A less effective protein knockdown at higher siRNA ratios can be explained by the specifics of GQD/siRNA complexation: larger amounts of siRNA may both generate a highly negative charge on the complex, hampering its internalization, and hinder the release of the neighboring siRNA sequences from the GQD surface. Furthermore, using high concentrations of siRNA could lead to off-target effects.[77] Similarly to EGFR knockdown, the expression of the KRAS protein is also inhibited by NGQD/siKRAS and Nd-NGQD/siKRAS complexes, with nearly maximum inhibition down to 51.5 ± 12.0 and $45.3 \pm 14.4\%$ observed at a 1:0.01 GQD/siRNA weight ratio, respectively (Figure 7b). This inhibition is comparable to the effect of the Lipofectamine positive control. It is noteworthy that KRAS knockdown does not exhibit substantial dependence on the platform type or the weight ratio between GQDs and siRNAs. Given the successful inhibition of KRAS and EGFR at nanomolar gene concentrations down to 31–36% and 45–51%, respectively, GQD/siRNA complexes can be further utilized as new promising therapeutic tools in cancer treatment.

4. CONCLUSIONS

In this work, highly biocompatible near-infrared-emissive graphene quantum dots are utilized for the first time as nanocarriers for RNA interference therapy. Nitrogen-doped and neodymium-doped graphene quantum dots (NGQDs and Nd-NGQDs, respectively) are synthesized via a cost-effective and scalable hydrothermal microwave-assisted approach with a single glucosamine carbon precursor. The resulting few nanometer-sized GQD structures exhibit intrinsic visible fluorescence, as well as fluorescence in the NIR region arising from the neodymium dopants. Both NGQDs and Nd-NGQDs form complexes

with siEGFR and siKRAS, as confirmed by ζ potentials and gel retardation assays, with electrostatically most efficient complexation at a 1:0.01 GQDs/siRNA weight ratio. Theoretical geometry optimization calculation reveals plausible GQD/siRNA complex structures that possess the potential for electrostatic interaction. TEM and HRTEM images confirm the presence of larger structures that can represent modeled complexes. NGQD/siEGFR, Nd-NGQD/siEGFR, NGQD/siKRAS, and Nd-NGQD/siKRAS hybrids at a 1:0.01 weight ratio demonstrate high biocompatibility at 375 μg/mL GQD concentration and successful internalization into HeLa cells, confirmed by confocal fluorescence microscopy, accumulating mostly in the cytoplasm. Within the cells, GQD/siRNA complexes facilitate substantial inhibition of EGFR and KRAS protein expression down to 31–45%, which for Nd-NGQD/siKRAS delivery is comparable to, or may surpass, the knockdown levels achieved with Lipofectamine 3000. Unlike Lipofectamine 3000, Nd-NGQDs can also perform NIR fluorescence imaging in HeLa cells with 808 nm laser excitation, showing their potential for *in vivo* gene delivery with NIR image tracking. Overall, both NGQDs and Nd-NGQDs are demonstrated here as successful nanocarriers that facilitate image-guided *in vitro* anticancer siRNA delivery with corresponding gene knockdown.

Supplementary Material

Refer to Web version on PubMed Central for supplementary material.

ACKNOWLEDGMENTS

REFERENCES

(1). Siegel RL; Miller KD; Fuchs HE; Jemal A. Cancer statistics, 2021. Ca Cancer J. Clin. 2021, 71, 7–33. [PubMed: 33433946]

(2). Dalmartello M; La Vecchia C; Bertuccio P; Boffetta P; Levi F; Negri E; Malvezzi M. European cancer mortality predictions for the year 2022 with focus on ovarian cancer. Ann. Oncol. 2022, 33, 330–339. [PubMed: 35090748]

(3). Takeshima H; Ushijima T. Accumulation of genetic and epigenetic alterations in normal cells and cancer risk. NPJ Precis. Oncol. 2019, 3, 1–8. [PubMed: 30623031]

(4). Song P; Yang F; Jin H; Wang X. The regulation of protein translation and its implications for cancer. Sig. Transduct. Targeted Ther. 2021, 6, No. 68.

(5). Timar J; Kashofer K. Molecular epidemiology and diagnostics of KRAS mutations in human cancer. Cancer Metastasis Rev. 2020, 39, 1029–1038. [PubMed: 32725342]

(6). Pinheiro G; Pereira T; Dias C; Freitas C; Hespanhol V; Costa JL; Cunha A; Oliveira HP Identifying relationships between imaging phenotypes and lung cancer-related mutation status: EGFR and KRAS. Sci. Rep. 2020, 10, No. 3625. [PubMed: 32107398]

(7). Sigismund S; Avanzato D; Lanzetti L. Emerging functions of the EGFR in cancer. Mol. Oncol. 2018, 12, 3–20. [PubMed: 29124875]

(8). Hamarsheh S; Groß O; Brummer T; Zeiser R. Immune modulatory effects of oncogenic KRAS in cancer. Nat. Commun. 2020, 11, No. 5439. [PubMed: 33116132]

(9). Plattner C; Hackl H. Modeling therapy resistance via the EGFR signaling pathway. FEBS J. 2019, 286, 1284–1286. [PubMed: 30892828]

(10). Leonetti A; Sharma S; Minari R; Perego P; Giovannetti E; Tiseo M. Resistance mechanisms to osimertinib in EGFR-mutated non-small cell lung cancer. Br. J. Cancer 2019, 121, 725–737. [PubMed: 31564718]

(11). Yuan XH; Yang J; Wang XY; Zhang XL; Qin TT; Li K. Association between EGFR/KRAS mutation and expression of VEGFA, VEGFR and VEGFR2 in lung adenocarcinoma. Oncol. Lett. 2018, 16, 2105–2112. [PubMed: 30008907]

(12). Xu W; Jiang X; Huang L. RNA interference technology. Comprehen. Biotechnol. 2019, 560.

(13). Ho VWT; Tan HY; Wang N; Feng Y. Cancer Management by Tyrosine Kinase Inhibitors: Efficacy, Limitation, and Future Strategies. In Tyrosine Kinases as Druggable Targets in Cancer; IntechOpen, 2019.

(14). Dana H; Chalbatani GM; Mahmoodzadeh H; Karimloo R; Rezaian O; Moradzadeh A; Mehmandoost N; Moazzen F; Mazraeh A; Marmari V. Molecular mechanisms and biological functions of siRNA. Int. J. Biomed. Sci. 2017, 13, 48–57. [PubMed: 28824341]

(15). Padda IS; Mahtani AU; Parmar M. Small Interfering RNA (siRNA) Based Therapy. In StatPearls [Internet]; StatPearls Publishing, 2022.

(16). Kim B; Park JH; Sailor MJ Rekindling RNAi therapy: materials design requirements for in vivo siRNA delivery. Adv. Mater. 2019, 31, No. 1903637.

(17). Paunovska K; Loughrey D; Dahlman JE Drug delivery systems for RNA therapeutics. Nat. Rev. Genet. 2022, 23, 265–280. [PubMed: 34983972]

(18). Shirley JL; de Jong YP; Terhorst C; Herzog RW Immune responses to viral gene therapy vectors. Mol. Ther. 2020, 28, 709–722. [PubMed: 31968213]

(19). Yan Y; Liu X-Y; Lu A; Wang X-Y; Jiang L-X; Wang J-C Non-viral vectors for RNA delivery. J. Controlled Release 2022, 342, 241–279.

(20). Thi TTH; Suys EJ; Lee JS; Nguyen DH; Park KD; Truong NP Lipid-based nanoparticles in the clinic and clinical trials: from cancer nanomedicine to COVID-19 vaccines. Vaccines 2021, 9, 359. [PubMed: 33918072]

(21). Torres-Vanegas JD; Cruz JC; Reyes LH Delivery systems for nucleic acids and proteins: Barriers, cell capture pathways and nanocarriers. Pharmaceutics 2021, 13, 428. [PubMed: 33809969]

(22). Gao H; Cheng R; A Santos H. Nanoparticle-mediated siRNA delivery systems for cancer therapy. View 2021, 2, No. 20200111.

(23). Li D; Gao C; Kuang M; Xu M; Wang B; Luo Y; Teng L; Xie J. Nanoparticles as drug delivery systems of RNAi in cancer therapy. Molecules 2021, 26, 2380. [PubMed: 33921892]

(24). Artiga Á; Serrano-Sevilla I; De Matteis L; Mitchell SG; Jesús M. Current status and future perspectives of gold nanoparticle vectors for siRNA delivery. J. Mater. Chem. B 2019, 7, 876–896. [PubMed: 32255093]

(25). Kong L; Qiu J; Sun W; Yang J; Shen M; Wang L; Shi X. Multifunctional PEI-entrapped gold nanoparticles enable efficient delivery of therapeutic siRNA into glioblastoma cells. Biomater. Sci. 2017, 5, 258–266. [PubMed: 27921110]

(26). Rahme K; Guo J; Holmes JD Bioconjugated gold nanoparticles enhance siRNA delivery in prostate cancer cells. In RNA Interference and Cancer Therapy; Springer, 2019; pp 291–301.

(27). Schwarz B; Merkel OM Functionalized PEI and its role in gene therapy. Mater Matters 2017, 12, 2.

(28). Zare H; Ahmadi S; Ghasemi A; Ghanbari M; Rabiee N; Bagherzadeh M; Karimi M; Webster TJ; Hamblin MR; Mostafavi E. Carbon nanotubes: Smart drug/gene delivery carriers. Int. J. Nanomed. 2021, 16, 1681.

(29). Amenta V; Aschberger K. Carbon nanotubes: potential medical applications and safety concerns. Wiley Interdiscip. Rev.: Nanomed. Nanobiotechnol. 2015, 7, 371–386. [PubMed: 25429905]

(30). Nißler R; Kurth L; Li H; Spreinat A; Kuhlemann I; Flavel BS; Kruss S. Sensing with chirality-pure near-infrared fluorescent carbon nanotubes. Anal. Chem. 2021, 93, 6446–6455. [PubMed: 33830740]

(31). Wang T; Chen Y; Wang B; Gao X; Wu M. Recent Progress in Second Near-Infrared (NIR-II) Fluorescence Imaging in Cancer. Biomolecules 2022, 12, 1044. [PubMed: 36008937]

(32). Kirkpatrick DL; Weiss M; Naumov A; Bartholomeusz G; Weisman RB; Gliko O. Carbon nanotubes: solution for the therapeutic delivery of siRNA? Materials 2012, 5, 278–301. [PubMed: 28817045]

(33). Demirer GS; Zhang H; Goh NS; Pinals RL; Chang R; Landry MP Carbon nanocarriers deliver siRNA to intact plant cells for efficient gene knockdown. Sci. Adv. 2020, 6, No. eaaz0495. [PubMed: 32637592]

(34). Campbell E; Hasan M; Pho C; Callaghan K; Akkaraju GR; Naumov AV Graphene oxide as a multifunctional platform for intracellular delivery, imaging, and cancer sensing. Sci. Rep. 2019, 9, No. 416. [PubMed: 30674914]

(35). Wang Y; Sun G; Gong Y; Zhang Y; Liang X; Yang L. Functionalized folate-modified graphene oxide/PEI siRNA nanocomplexes for targeted ovarian cancer gene therapy. Nanoscale Res. Lett. 2020, 15, No. 57. [PubMed: 32140846]

(36). Chen S; Zhang S; Wang Y; Yang X; Yang H; Cui C. AntiEpCAM functionalized graphene oxide vector for tumor targeted siRNA delivery and cancer therapy. Asian J. Pharm. Sci. 2021, 16, 598–611. [PubMed: 34849165]

(37). Murjani BO; Kadu PS; Bansod M; Vaidya SS; Yadav MD Carbon nanotubes in biomedical applications: current status, promises, and challenges. Carbon Lett. 2022, 32, 1207–1226.

(38). Ghulam AN; dos Santos OA; Hazeem L; Pizzorno Backx B; Bououdina M; Bellucci S. Graphene Oxide (GO) Materials-Applications and Toxicity on Living Organisms and Environment. J. Funct. Biomater. 2022, 13, No. 77. [PubMed: 35735932]

(39). Zhao C; Song X; Liu Y; Fu Y; Ye L; Wang N; Wang F; Li L; Mohammadniaei M; Zhang M; et al. Synthesis of graphene quantum dots and their applications in drug delivery. J. Nanobiotechnol. 2020, 18, No. 142.

(40). Biswas MC; Islam MT; Nandy PK; Hossain MM Graphene Quantum Dots (GQDs) for Bioimaging and Drug Delivery Applications: A Review. ACS Mater. Lett. 2021, 3, 889–911.

(41). Younis MR; He G; Lin J; Huang P. Recent advances on graphene quantum dots for bioimaging applications. Front. Chem. 2020, 8, 424. [PubMed: 32582629]

(42). Perini G; Palmieri V; Ciasca G; De Spirito M; Papi M. Unravelling the potential of graphene quantum dots in biomedicine and neuroscience. Int. J. Mol. Sci. 2020, 21, No. 3712. [PubMed: 32466154]

(43). Frieler M; Pho C; Lee BH; Dobrovolny H; Akkaraju GR; Naumov AV Effects of doxorubicin delivery by nitrogen-doped graphene quantum dots on cancer cell growth: experimental study and mathematical modeling. Nanomaterials 2021, 11, No. 140. [PubMed: 33435595]

(44). Liang J; Liu J; Jin X; Yao S; Chen B; Huang Q; Hu J; Wan J; Hu Z; Wang B. Versatile nanoplatform loaded with doxorubicin and graphene quantum dots/methylene blue for drug delivery and chemophotothermal/photodynamic synergetic cancer therapy. ACS Appl. Bio Mater. 2020, 3, 7122–7132.

(45). Ghafary SM; Nikkhah M; Hatamie S; Hosseinkhani S. Simultaneous gene delivery and tracking through preparation of photo-luminescent nanoparticles based on graphene quantum dots and chimeric peptides. Sci. Rep. 2017, 7, No. 9552. [PubMed: 28842617]

(46). Hai X; Feng J; Chen X; Wang J. Tuning the optical properties of graphene quantum dots for biosensing and bioimaging. J. Mater. Chem. B 2018, 6, 3219–3234. [PubMed: 32254380]

(47). Kansara V; Shukla R; Flora SJS; Bahadur P; Tiwari S. Graphene quantum dots: synthesis, optical properties and navigational applications against cancer. Mater. Today Commun. 2022, 31, No. 103359.

(48). Li G; Liu Y; Niu J; Pei M; Lin W. A ratiometric fluorescent composite nanomaterial for RNA detection based on graphene quantum dots and molecular probes. J. Mater. Chem. B 2018, 6, 4380–4384. [PubMed: 32254513]

(49). Jeong S; Pinals RL; Dharmadhikari B; Song H; Kalluri A; Debnath D; Wu Q; Ham M-H; Patra P; Landry MP. Graphene Quantum Dot Oxidation Governs Noncovalent Biopolymer Adsorption. Scientific Reports 2020, 10 (1), 7074. [PubMed: 32341425]

(50). Ajgaonkar R; Lee B; Valimukhametova A; Nguyen S; Gonzalez-Rodriguez R; Coffer J; Akkaraju GR; Naumov AV Detection of pancreatic cancer miRNA with biocompatible nitrogen-doped graphene quantum dots. Materials 2022, 15, 5760. [PubMed: 36013894]

(51). Wu C; Song X; Song Z; He Z; Dai J. Ultrasensitive detection of protein based on graphene quantum dots with resonance light scattering technique. J. Nanosci. Nanotechnol. 2018, 18, 2680–2685. [PubMed: 29442943]

(52). Xu A; He P; Huang T; Li J; Hu X; Xiang P; Chen D; Yang S; Wang G; Ding G. Selective supramolecular interaction of ethylenediamine functionalized graphene quantum dots: Ultrasensitive photoluminescence detection for nickel ion in vitro. Synth. Met. 2018, 244, 106–112.

(53). Chung S; Revia RA; Zhang M. Graphene quantum dots and their applications in bioimaging, biosensing, and therapy. Adv. Mater. 2021, 33, No. 1904362.

(54). Wang J; Liu S; Chang Y; Fang L; Han K; Li M. High efficient delivery of siRNA into tumor cells by positively charged carbon dots. J. Macromol. Sci., Part A 2018, 55, 770–774.

(55). Zhao X; Yang J; Wang X; Chen L; Zhang C; Shen Z. Inhibitory effect of aptamer-carbon dot nanomaterial-siRNA complex on the metastasis of hepatocellular carcinoma cells by interfering with FMRP. Eur. J. Pharm. Biopharm. 2022, 174, 47–55. [PubMed: 35364257]

(56). Wang Q; Zhang C; Shen G; Liu H; Fu H; Cui D. Fluorescent carbon dots as an efficient siRNA nanocarrier for its interference therapy in gastric cancer cells. J. Nanobiotechnol. 2014, 12, No. 58.

(57). Li R; Wei F; Wu X; Zhou P; Chen Q; Cen Y; Xu G; Cheng X; Zhang A; Hu Q. PEI modified orange emissive carbon dots with excitation-independent fluorescence emission for cellular imaging and siRNA delivery. Carbon 2021, 177, 403–411.

(58). Kim S; Choi Y; Park G; Won C; Park Y-J; Lee Y; Kim B-S; Min D-H Highly efficient gene silencing and bioimaging based on fluorescent carbon dots in vitro and in vivo. Nano Res. 2017, 10, 503–519.

(59). Campbell E; Hasan MT; Gonzalez Rodriguez R; Akkaraju GR; Naumov AV Doped graphene quantum dots for intracellular multicolor imaging and cancer detection. ACS Biomater. Sci. Eng. 2019, 5, 4671–4682. [PubMed: 33448839]

(60). Hasan MT; Gonzalez-Rodriguez R; Lin CW; Campbell E; Vasireddy S; Tsedev U; Belcher AM; Naumov AV Rare-earth metal ions doped graphene quantum dots for near-ir in vitro/in vivo/ex vivo imaging applications. Adv. Opt. Mater. 2020, 8, No. 2000897.

(61). Hanwell MD; Curtis DE; Lonie DC; Vandermeersch T; Zurek E; Hutchison GR Avogadro: an advanced semantic chemical editor, visualization, and analysis platform. J. Cheminf. 2012, 4, No. 17.

(62). Halgren TA Merck molecular force field. I. Basis, form, scope, parameterization, and performance of MMFF94. J. Comput. Chem. 1996, 17, 490–519.

(63). Hasan MT; Gonzalez-Rodriguez R; Ryan C; Faerber N; Coffer JL; Naumov AV Photo-and electroluminescence from nitrogen-doped and nitrogen–sulfur codoped graphene quantum dots. Adv. Funct. Mater. 2018, 28, No. 1804337.

(64). Wang L; Wang Y; Xu T; Liao H; Yao C; Liu Y; Li Z; Chen Z; Pan D; Sun L; Wu M. Gram-scale synthesis of single-crystalline graphene quantum dots with superior optical properties. Nat. Commun. 2014, 5, No. 5357. [PubMed: 25348348]

(65). Valimukhametova AR; Zub OS; Lee BH; Fannon O; Nguyen S; Gonzalez-Rodriguez R; Akkaraju GR; Naumov AV Dual-Mode Fluorescence/Ultrasound Imaging with Biocompatible Metal-Doped Graphene Quantum Dots. ACS Biomater. Sci. Eng. 2022, 8, 4965–4975. [PubMed: 36179254]

(66). Campbell E; Hasan MT; Gonzalez-Rodriguez R; Truly T; Lee BH; Green KN; Akkaraju G; Naumov AV Graphene quantum dot formulation for cancer imaging and redox-based drug delivery. Nanomed.: Nanotechnol. Biol. Med. 2021, 37, No. 102408.

(67). Ben Aoun S. Nanostructured carbon electrode modified with N-doped graphene quantum dots–chitosan nanocomposite: a sensitive electrochemical dopamine sensor. R. Soc. Open Sci. 2017, 4, No. 171199. [PubMed: 29291105]

(68). Baskoro F; Wong C-B; Kumar SR; Chang C-W; Chen C-H; Chen DW; Lue SJ Graphene oxide-cation interaction: Inter-layer spacing and zeta potential changes in response to various salt solutions. J. Membr. Sci. 2018, 554, 253–263.

(69). Aydin O; Kanarya D; Yilmaz U; Tunc CÜ Determination of Optimum Ratio of Cationic Polymers and Small Interfering RNA with Agarose Gel Retardation Assay. In Antisense RNA Design, Delivery, and Analysis; Humana: New York, NY, 2022; pp 117–128.

(70). Fröhlich E. The role of surface charge in cellular uptake and cytotoxicity of medical nanoparticles. Int. J. Nanomed. 2012, 7, 5577.

(71). Ramana LN; Dinh LN; Agarwal V. Influence of surface charge of graphene quantum dots on their uptake and clearance in melanoma cells. Nanoscale Adv. 2021, 3, 3513–3521. [PubMed: 36133718]

(72). Halder A; Godoy-Gallardo M; Ashley J; Feng X; Zhou T; Hosta-Rigau L; Sun Y. One-pot green synthesis of biocompatible graphene quantum dots and their cell uptake studies. ACS Appl. Bio. Mater. 2018, 1, 452–461.

(73). Yuan X; Liu Z; Guo Z; Ji Y; Jin M; Wang X. Cellular distribution and cytotoxicity of graphene quantum dots with different functional groups. Nanoscale Res. Lett. 2014, 9, No. 108. [PubMed: 24597852]

(74). Berezhna SY; Supekova L; Supek F; Schultz PG; Deniz AA siRNA in human cells selectively localizes to target RNA sites. Proc. Natl. Acad. Sci. U.S.A. 2006, 103, 7682–7687. [PubMed: 16684885]

(75). Pinals RL; Yang D; Rosenberg DJ; Chaudhary T; Crothers AR; Iavarone AT; Hammel M; Landry MP Quantitative protein corona composition and dynamics on carbon nanotubes in biological environments. Angew. Chem., Int. Ed. 2020, 59, 23668–23677.

(76). Mahmood T; Yang P-C Western blot: technique, theory, and trouble shooting. North Am. J. Med. Sci. 2012, 4, 429.

(77). Caffrey DR; Zhao J; Song Z; Schaffer ME; Haney SA; Subramanian RR; Seymour AB; Hughes JD siRNA off-target effects can be reduced at concentrations that match their individual potency. PLoS One 2011, 6, No. e21503. [PubMed: 21750714]
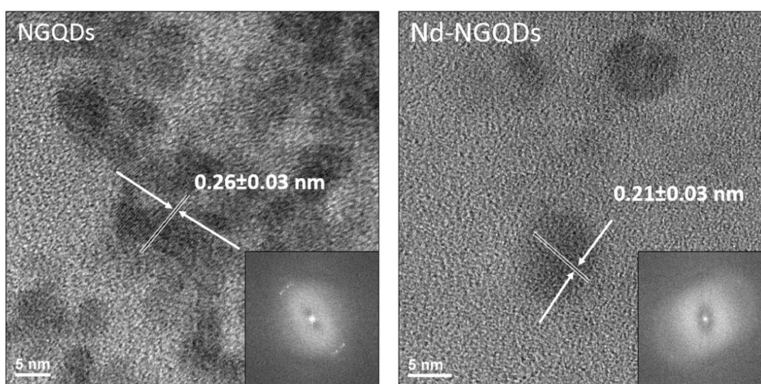
Figure 1.
HRTEM images of NGQDs (left panel) and Nd-NGQDs (right panel) with corresponding characteristic graphitic lattice spacings. Insets: FFT images.
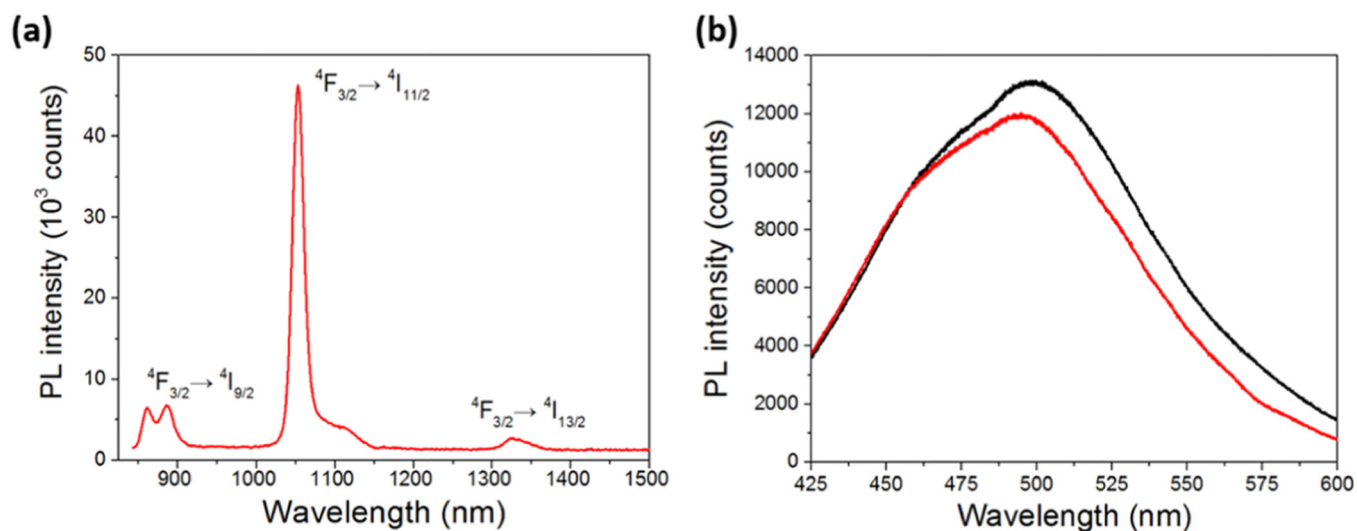
Figure 2.
(a) NIR fluorescence of Nd-NGQDs at a concentration of 11.3 mg/mL with 808 nm laser excitation. (b) Visible fluorescence of NGQDs (black) and Nd-NGQDs (red) at 10 and 11.3 mg/mL concentrations with 400 nm xenon lamp excitation.
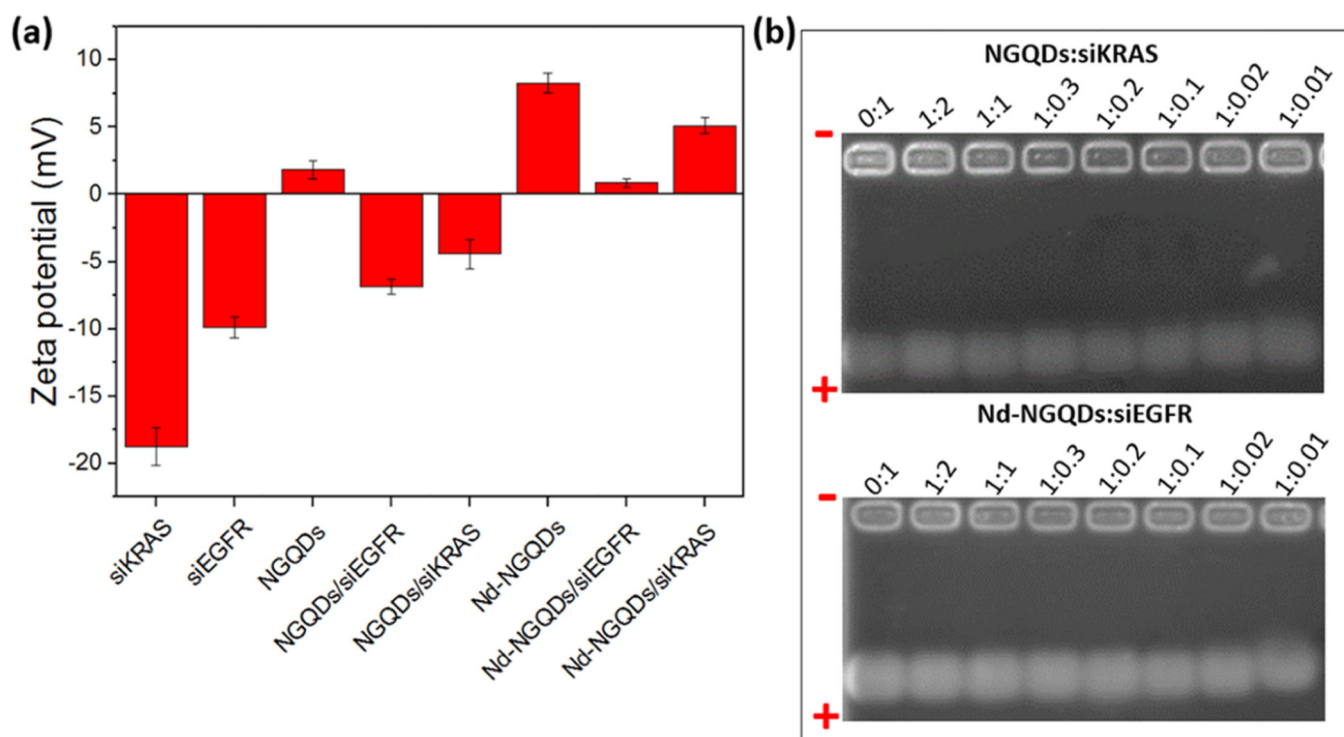
Figure 3.
(a) ζ potentials of siKRAS; siEGFR; NGQDs; Nd-NGQDs; and NGQD/siEGFR, NGQD/siKRAS, Nd-NGQD/siEGFR, and Nd-NGQD/siKRAS complexes at a 1:0.01 w/w ratio. (b) Gel retardation assay of NGQD/siKRAS and Nd-NGQD/siEGFR complexes at different w/w ratios.
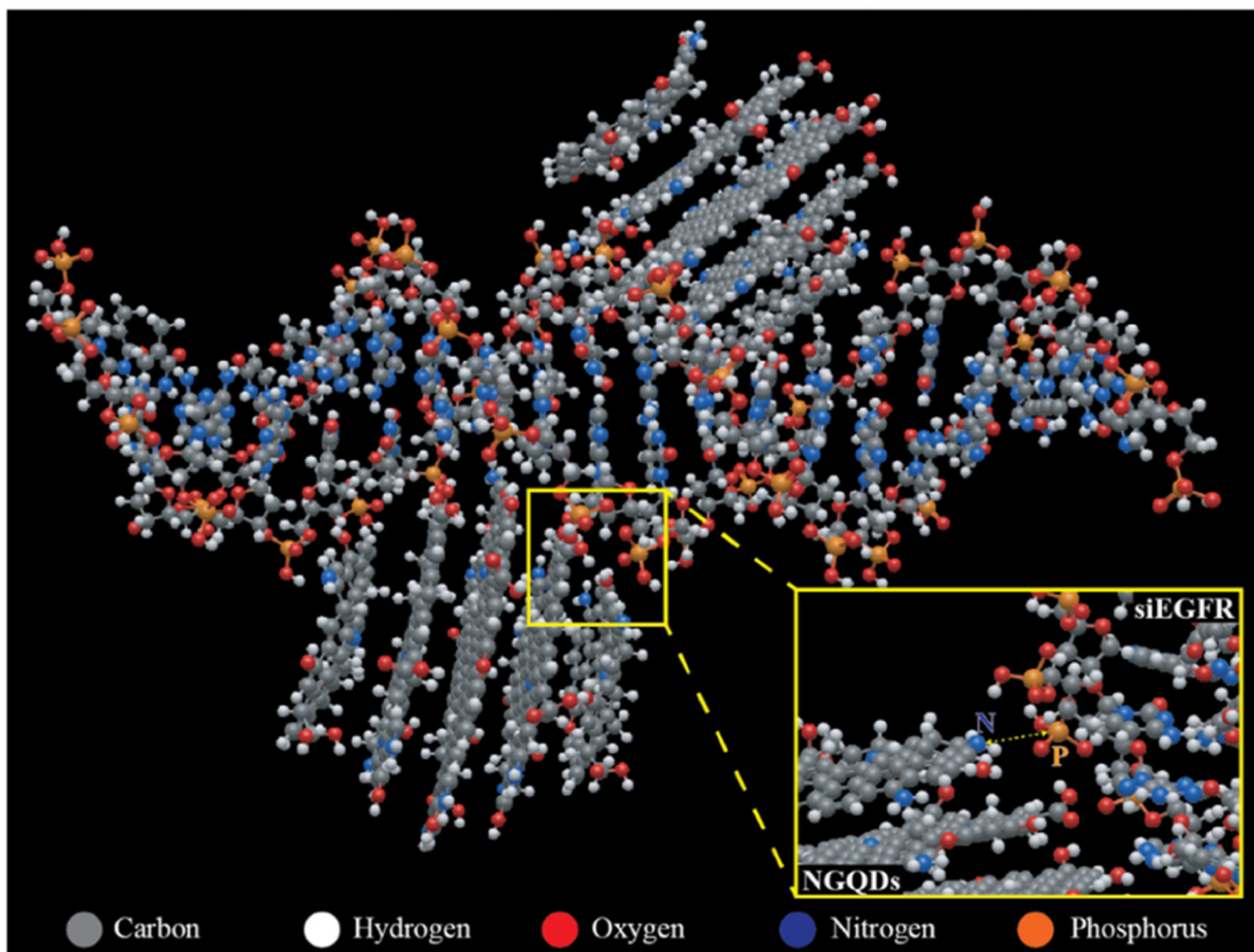
Figure 4.
Molecular visualization of the NGQD/siEGFR complex geometrically optimized with the MMFF94 energy minimization calculation. Inset: zoomed-in area showing the proximity of amino groups of NGQDs and phosphate groups of siEGFR.
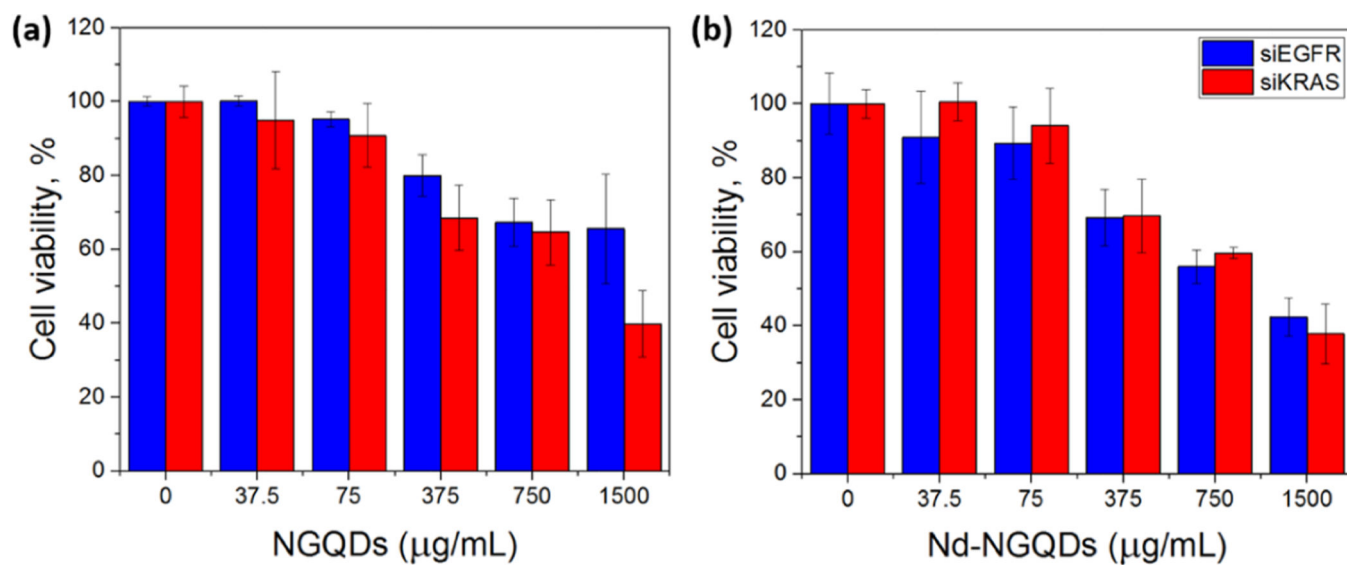
Figure 5.

Cell viability of HeLa cells after treatment with (a) NGQD/siEGFR and NGQD/siKRAS and (b) Nd-NGQD/siEGFR and Nd-NGQD/siKRAS complexes at a 1:0.01 weight ratio.
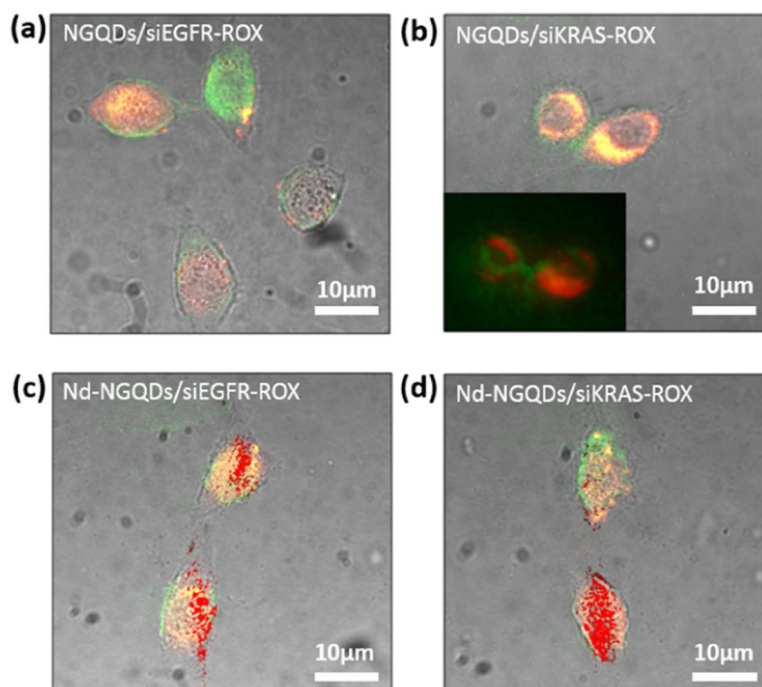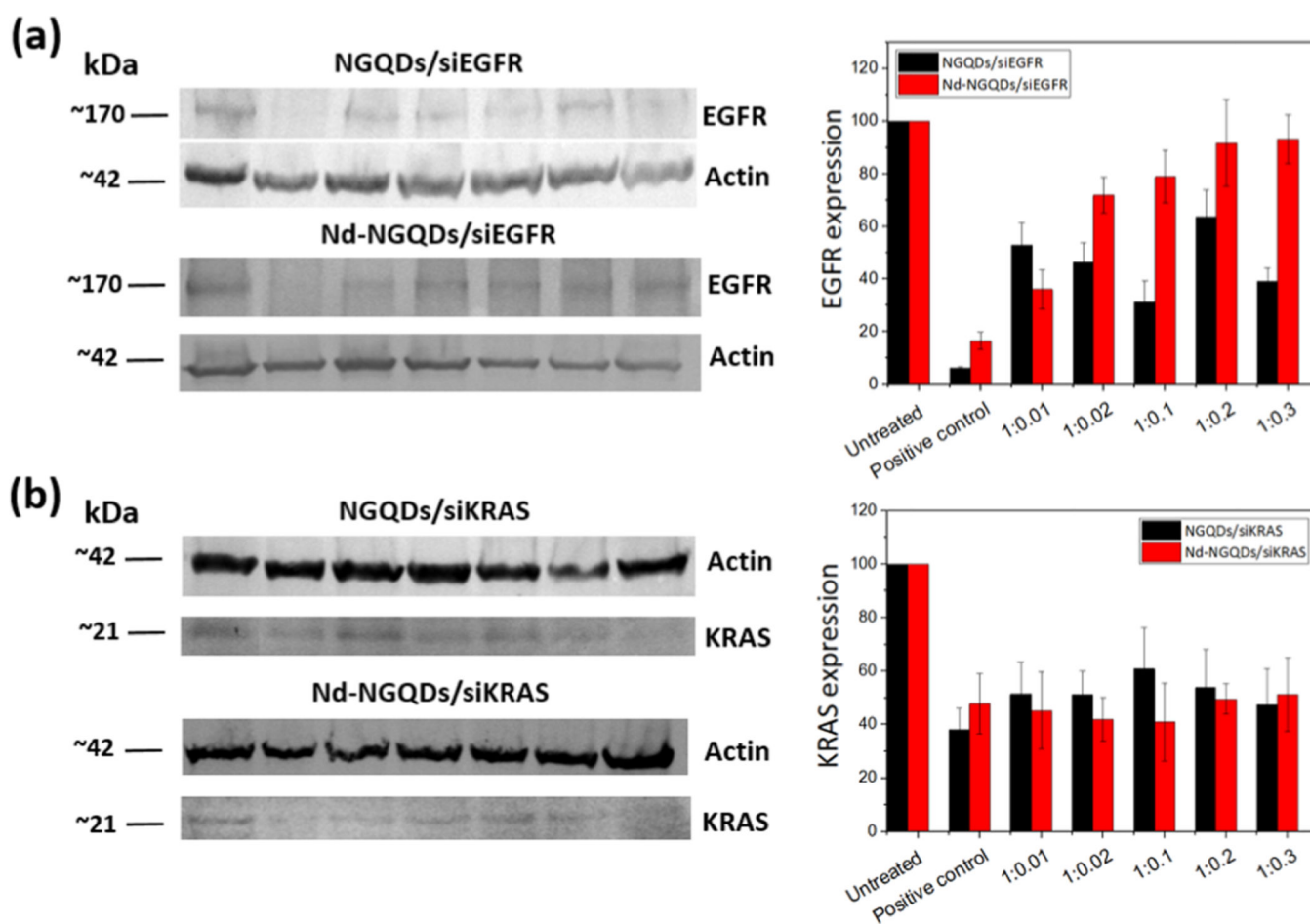
Figure 6.
Bright-field/visible fluorescence confocal overlay images of HeLa cells treated with (a) NGQDs/siEGFR-ROX, (b) NGQDs/siKRAS-ROX, (c) NGQDs/siEGFR-ROX, and (d) Nd-NGQDs/siKRAS-ROX for 12 h. GQD (shown in green) is excited with 480 ± 20 nm and collected at 535 ± 20 nm, and ROX (shown in orange) is excited with 540 ± 20 nm and collected at 600 ± 20 nm. Panels (c) and (d) also include the overlay of NIR fluorescence arising from internalized Nd-NGQDs. Nd-NGQD (shown in red) is excited with an 808 nm laser and collected in the range of 850–1350 nm. Panel (b) inset: 3D confocal image of green GQD and orange ROX fluorescence in the HeLa cells treated with NGQDs/siKRAS-ROX.

Figure 7.
Representative western blot images and quantification of the blots upon treatment of HeLa cells with (a) NGQD/siEGFR and Nd-NGQD/siEGFR and (b) NGQD/siKRAS and Nd-NGQD/siKRAS complexes at different GQD/siRNA weight ratios. Lipofectamine 3000 is used as a positive control. EGFR and KRAS protein expression is normalized by actin protein loading and presented as a percentage of the untreated sample. Values represent the mean ± SE of three independent experiments.